JACS Au
AN OPEN ACCESS JOURNAL OF THE AMERICAN CHEMICAL SOCIETY



pubs.acs.org/jacsau
Article

# Two-Dimensional MOF Constructed by a Binuclear-Copper Motif for High-Performance Electrocatalytic NO Reduction to $NH_3$

Rong Luo,[¶] Bao-Jing Li,[¶] Zhan-Peng Wang,[¶] Ming-Guang Chen, Gui-Lin Zhuang,* Quan Li, Jia-Ping Tong, Wen-Tai Wang,* Yu-Hua Fan, and Feng Shao*

Cite This: *JACS Au* 2024, 4, 3823−3832



**ABSTRACT:** Ambient electrochemical NO reduction presents a dual solution for sustainable NO reduction and $NH_3$ synthesis. However, their complex kinetics and energy demands necessitate high-performance electrocatalysts to ensure effective and selective process outcomes. Herein, we report that a two-dimensional Cu-based metal−organic framework (MOF), $\{[Cu(HL)]\cdot H_2O\}_n$, (**Cu-OUC**, $H_3L$ = 5-(2′-carboxylphenoxy)isophthalic acid) acts as a stable electrocatalyst with high efficiency for NO-to-$NH_3$ conversion. Electrochemical experimental studies showed that in 0.1 M $K_2SO_4$ solution, the as-prepared **Cu-OUC** achieved a peak Faradaic efficiency of 96.91% and a notable $NH_3$ yield as high as 3415.82 $\mu$g $h^{-1}$ $mg^{-1}$. The Zn−NO battery in aqueous solution can produce electricity possessing a power density of 2.04 mW $cm^{-2}$ while simultaneously achieving an $NH_3$ yield of 616.92 $\mu$g $h^{-1}$ $mg^{-1}$. Theoretical calculations revealed that the surface of **Cu-OUC** effectively facilitates NO activation through a two-way charge transfer mechanism of "electron acceptance and donation", with the *NO formation step being the potential-determining stage. The study pioneers the use of a MOF as an electrocatalyst for ambient NO-to-$NH_3$ conversion.

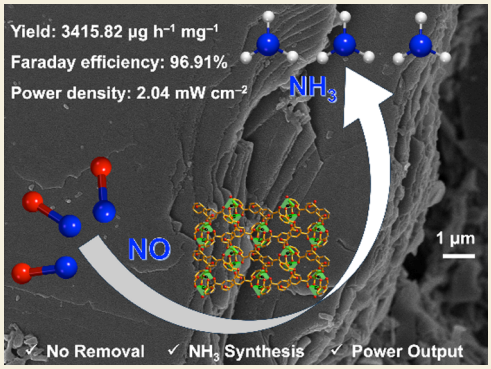


**KEYWORDS:** *Metal−Organic Framework, Electrocatalyst, Nitric Oxide (NO), Ammonia ($NH_3$), Theoretical Calculations*

## INTRODUCTION

Ammonia ($NH_3$) is the second-most manufactured synthetic chemical, plays a critical role in sustaining human life, and is also regarded as an attractive carbon-neutral energy carrier owning high hydrogen capacity.[1−3] The current industrial $NH_3$ production through the Haber−Bosch process is highly energy-intensive and causes a lot of greenhouse gas emissions.[4−6] To settle these issues, many researchers have devoted themselves to finding an environment-friendly and sustainable alternative for $NH_3$ synthesis as a potential alternative to the Haber−Bosch process.[7−10] Recently, the electrochemical nitrogen ($N_2$) reduction reaction (NRR) is an energy-efficient and eco-friendly method that requires only $N_2$ and $H_2O$ for $NH_3$ production and has attracted paramount attention from researchers.[11−14] However, owing to the chemical inertness of nonpolar $N_2$, intrinsically sluggish kinetics, and the competing hydrogen evaluation reaction (HER), the NRR encounters issues with activity and selectivity, making electrochemical $NH_3$ synthesis from $N_2$ a continuing challenge.[15,16] Encouragingly, compared with the NRR process, the electrochemical nitric oxide (NO) reduction reaction (NORR) is kinetically and thermodynamically relatively easy for $NH_3$ synthesis because of the lower dissociation energy of NO.[17−22] Besides, NO is one of the major man-made atmospheric pollutants, resulting in environmental issues and thus threatening public health.[23,24] Hence, the NORR holds great promise to realize simultaneously green $NH_3$ synthesis and harmful NO removal. The complicated five-electron process and competitive HER process of the NORR highlight the key role of electrocatalysts. And the development of efficient electrocatalysts has indeed been a technological bottleneck, limiting the large-scale practical applications of ammonia synthesis via the NORR.[25,26]

Two-dimensional (2D) materials have increasingly attracted significant attention as potential materials for energy storage and conversion devices owing to their distinct optical and electrical properties.[27−29] In contrast to inorganic 2D materials (such as graphene, 2D metal sulfides, and 2D metal oxides), 2D MOFs can be synthesized by the self-assembly of selectable metal nodes and designable organic ligands, resulting in a variety of structural motifs. The well-defined structure has contributed to studying the mechanism and comprehending the structure−activity relationship. Furthermore, the intrinsic properties of 2D

Received: June 4, 2024
Revised: September 19, 2024
Accepted: September 19, 2024
Published: October 1, 2024





https://doi.org/10.1021/jacsau.4c00475
*JACS Au* 2024, 4, 3823−3832

MOFs including ultrathin layer thickness, tunable pore structure, and extremely high specific surface area can afford open channels and uniform active sites for chemo-, size-, shape-, and stereoselective interactions, which are favorable to electron transport in the framework, giving them superior activity and cyclability.[30−32] Owing to the well-defined structures and designability, 2D MOFs have been proposed for various energy-conversion reactions.[30,33−39] For instance, Zhu et al.[37] reported the conductive Cu-based MOF (**CuHHTP**) composites for selective $NH_3$ production from $NO_3^-$ reduction. The Cu clusters are filled into the mesopores of **CuHHTP**; meanwhile, the porous structure of **CuHHTP** restricts the growth and aggregation of Cu clusters for its internal environment. Xu et al.[38] reported that ultrathin 2D Co-MOF nanosheets could exhibit an overpotential of 263 mV in the electrocatalytic oxygen evolution reaction (OER), which was attributed to the porous structure of ultrathin nanosheets and high accessibility of surface-active sites as well as excellent electron transfer and rapid mass transport. Li et al.[39] reported a helical rod-based 2D Bi-MOF featuring unique crystallographically independent channels for effective electrochemical carbon dioxide reduction to formic acid. However, to the best of our knowledge, 2D MOFs serving as electrocatalysts for NO conversion to $NH_3$ have not been experimentally explored by now. The development of high-performance 2D MOF-based catalysts has important scientific significance for advancing the electrochemical reduction of NO to $NH_3$.

Herein, a 2D copper-based MOF electrocatalyst, $\{[Cu(HL)]\cdot H_2O\}_n$ (**Cu-OUC**, $H_3L$ = 5-(2′-carboxylphenoxy)isophthalic acid), was obtained by the hydrothermal method for the direct electrochemical reduction of NO into $NH_3$ at ambient conditions. **Cu-OUC** exhibited an $NH_3$ yield as high as 3415.82 $\mu g\ h^{-1}\ mg_{cat}^{-1}$ in 0.1 M $K_2SO_4$ solution and gave a high Faradaic efficiency (FE) of up to 96.91% at −0.4 V versus a reversible hydrogen electrode and displayed outstanding stability for the NORR. Moreover, **Cu-OUC** can serve as the cathode material for Zn−NO primary batteries to facilitate the reduction of harmful NO into $NH_3$ while achieving high electricity generation. An in-depth insight into the catalytic NORR mechanism was stated by theoretical calculations.

## METHODS

### Synthesis of $\{[Cu(HL)]\cdot H_2O\}_n$ (Cu-OUC)

**Cu-OUC** was successfully prepared by a hydrothermal method. $CuCl_2$ (25.6 mg, 0.15 mmol), $H_3L$ (30.9 mg, 0.10 mmol), and 1,4-bis(lmidazol)butane (19.0 mg, 0.10 mmol) were dissolved in 8.0 mL of $H_2O$ and sonicated for 20 min at room temperature, then transferred to a sealed polytetrafluoroethylene reactor. The blue block crystals were obtained by keeping the reactor at 110 °C for 72 h and slowly cooling it to room temperature. The final **Cu-OUC** products were collected, washed with $H_2O$, and dried under a vacuum. Yield: 48.2% (based on Cu). Elemental analysis calculated: C 47.19, H 2.64. Found: C 47.21, H 2.59. FT-IR ($cm^{-1}$) (Figure S1): 3567 (s), 3462 (m), 2920 (s), 2823 (m), 2576 (m), 1701 (s), 1623 (s), 1586 (s), 1458 (s), 1397 (s), 1303 (s), 1253 (s), 1215 (w), 1163 (m), 1097 (m), 1031 (w), 1003 (w), 984 (s), 892 (s), 860 (w), 784 (m), 763 (s), 724 (w), 700 (m), 670 (m), 538 (w), 492 (s), 457 (m).

### Electrochemical NORR Measurements

Electrochemical measurements were conducted in a sealed single room electrolytic cell using a three-electrode system in NO-saturated 0.1 M $K_2SO_4$ solution at room temperature. **Cu-OUC** dropped on carbon paper (CP, 1 × 1 $cm^2$) served as the working electrode, with an Ag/AgCl (saturated KCl electrolyte) and platinum wire as the reference electrode and counter electrode, respectively. The electrolyte was purged with high-purity Ar gas (99.999%) for 30 min before the electrochemical tests to eliminate any air. Generally, 10 mg of **Cu-OUC** was ultrasonically dispersed in a mixture of Nafion solution (5 wt %, 50 $\mu$L) and EtOH (950 $\mu$L) to form a homogeneous suspension, then dropped (10 $\mu$L) onto the surface of carbon paper and dried at room temperature for 12 h.

## RESULTS AND DISCUSSION

### Crystal Structure of Cu-OUC

Single-crystal X-ray diffraction (SC-XRD) analysis (Table 1) revealed that **Cu-OUC** crystallized in the orthorhombic *Pbca* space group, which is comprised of $[Cu_2O_2(COO)_4]$ clusters and carboxylic acid linkers (Figure 1a). As shown in Figure 1b, the Cu(II) ion is coordinated with five oxygens from the carboxyl group from five different partially deprotonated ligands ($HL^{2-}$), forming a distorted pyramid geometry. Two equivalent Cu(II) ions are connected by four carboxylic groups to afford a binuclear paddlewheel copper cluster $[Cu_2O_2(COO)_4]$ as the secondary building unit (SBU), giving a Cu···Cu distance of 2.598 Å. The Cu−O bond distances lie in the range between 1.958 and 2.127 Å, which are similar to those observed in other reported Cu(II) compounds with carboxylate ligands (Table S1). In **Cu-OUC**, each $HL^{2-}$ ligand functions as a $\mu_5$-bridge to link five Cu(II) ions, in which two carboxylate groups adopt $\mu_2$-$\eta^1$:$\eta^1$-bis-monodentate modes, the other one adopts the coordination mode of $\mu_1$-$\eta^1$:$\eta^0$-monodentate (Figure 1c). On this basis, as illustrated in Figure 1d, each $HL^{2-}$ is linked to three SBUs and each SBU is linked to six $HL^{2-}$ ligands to give a 2D framework. The hydrogen bonding interactions (O6−H6···O3,

**Table 1. Crystallographic Data and Structure Refinement Parameters for Cu-OUC**

| complex | Cu-OUC |
|---|---|
| formula | $C_{15}H_{10}CuO_8$ |
| $M_w$ (g $mol^{-1}$) | 381.77 |
| crystal system | orthorhombic |
| space group | *Pbca* |
| temperature (K) | 170 |
| *a* (Å) | 12.8798(7) |
| *b* (Å) | 10.8893(6) |
| *c* (Å) | 20.8581(12) |
| $\alpha$ (deg) | 90 |
| $\beta$ (deg) | 90 |
| $\gamma$ (deg) | 90 |
| *V* ($Å^3$) | 2925.4(3) |
| *Z* | 8 |
| radiation type | Mo K$\alpha$ |
| *F* (000) | 1544 |
| $D_{calcd}$ (Mg $m^{-3}$) | 1.734 |
| $\theta$ range | 2.5−26.4° |
| $\mu$ ($mm^{-1}$) | 1.54 |
| reflections collected | 13616 |
| reflections with $I > 2\sigma(I)$ | 1938 |
| $R_{int}$ | 0.099 |
| GOF | 1.078 |
| parameters | 221 |
| final *R* indices ($I > 2\sigma(I)$)[a] | $R_1$ = 0.0511; $wR_2$ = 0.0876 |
| final *R* indices (all data)[a] | $R_1$ = 0.1018; $wR_2$ = 0.1149 |
| *S* (all data) | 1.08 |
| CCDC | 2288852 |

[a] $R_1 = \Sigma(||F_o| - |F_c||)/\Sigma|F_o|$, $wR_2 = [\Sigma w\ (F_o^2 - F_c^2)^2/\Sigma w(F_o^2)^2]^{0.5}$.



https://doi.org/10.1021/jacsau.4c00475
JACS Au 2024, 4, 3823−3832

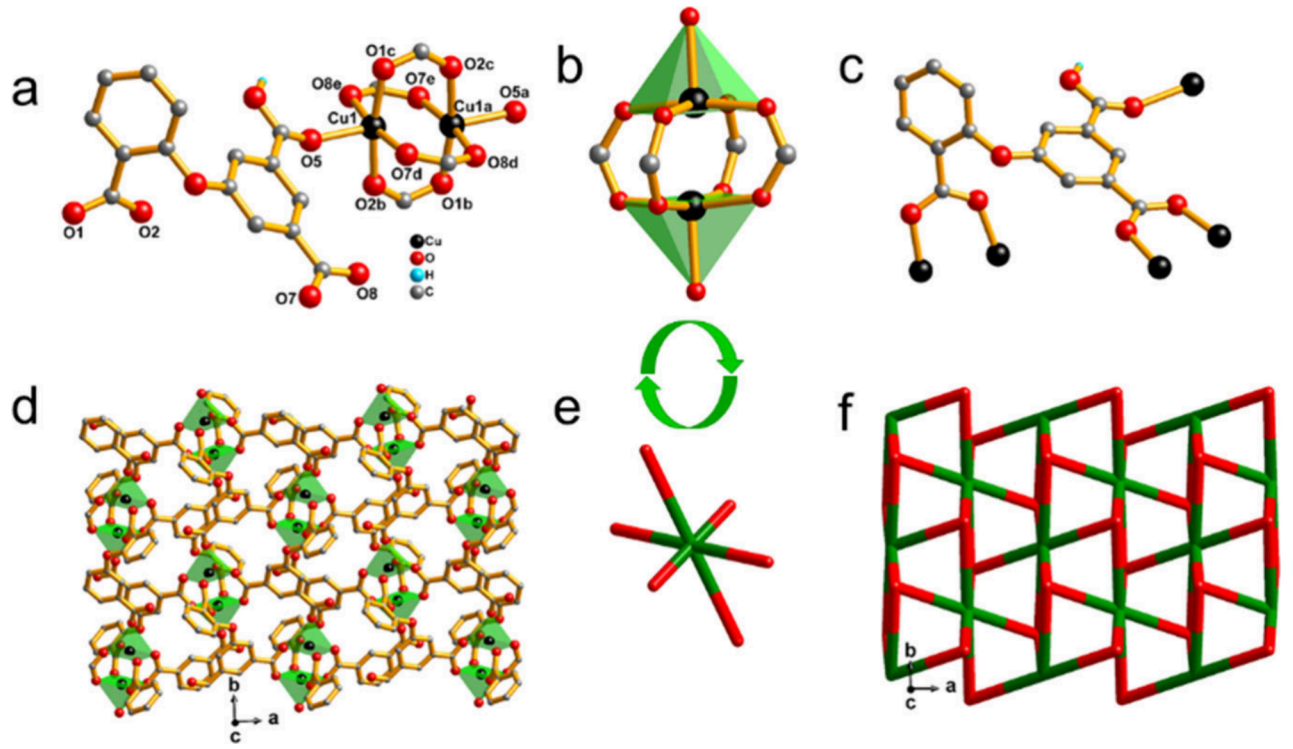


**Figure 1.** (a) Coordination environment of Cu(II) in **Cu-OUC** (all the H atoms were omitted for clarity). (b) SBU framework in **Cu-OUC**. (c) Coordination modes of $HL^{2-}$. (d) The 3D framework of view **Cu-OUC**. (e and f) 3D topology view of **Cu-OUC**.

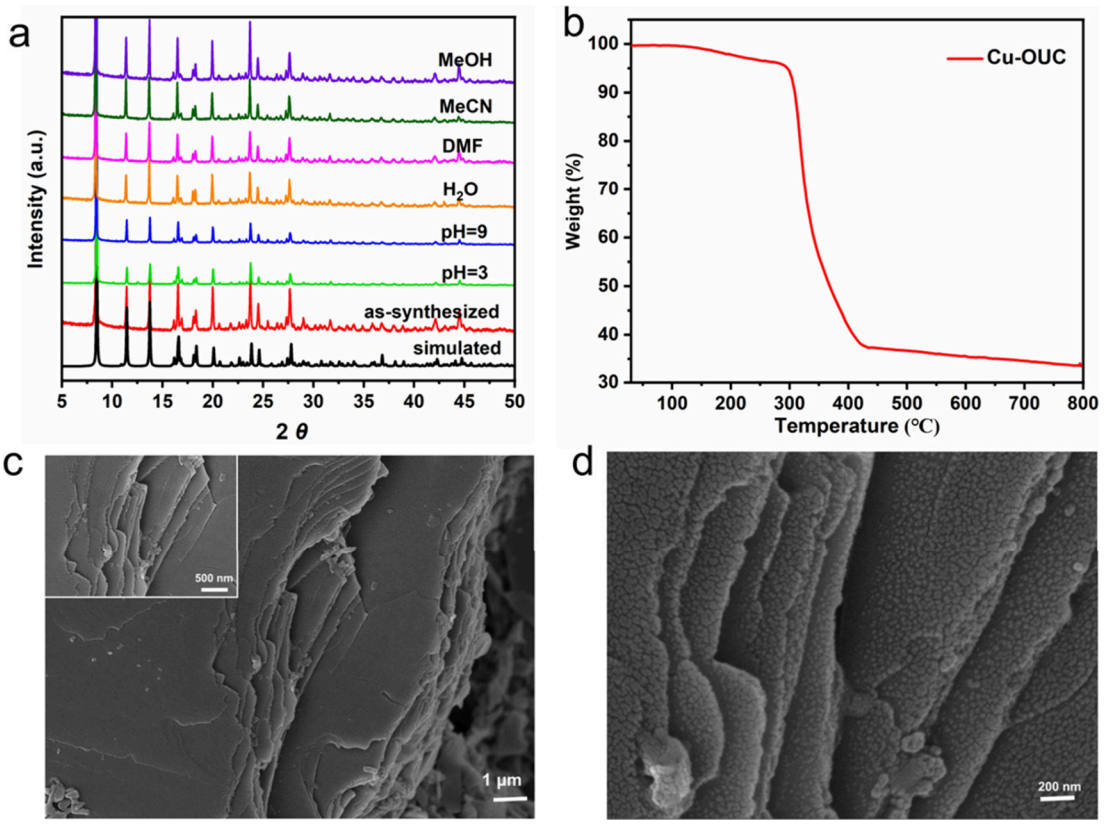


**Figure 2.** PXRD patterns (a), TGA curve (b), and SEM images (c and d) of **Cu-OUC**.

O3−H3A···O2, and O3−H3B···O8) further increase the stability of the 2D structure. The PLATON analysis showed that the total guest-accessible void space is 71.0 Å$^3$, which corresponds to 2.4% of the unit cell volume of 2928.4 Å$^3$.[40] From a topological perspective, the $[Cu_2O_2(COO)_4]$ SBU and the $HL^{2-}$ linker in the 2D layered structure can be respectively



https://doi.org/10.1021/jacsau.4c00475
JACS Au 2024, 4, 3823−3832

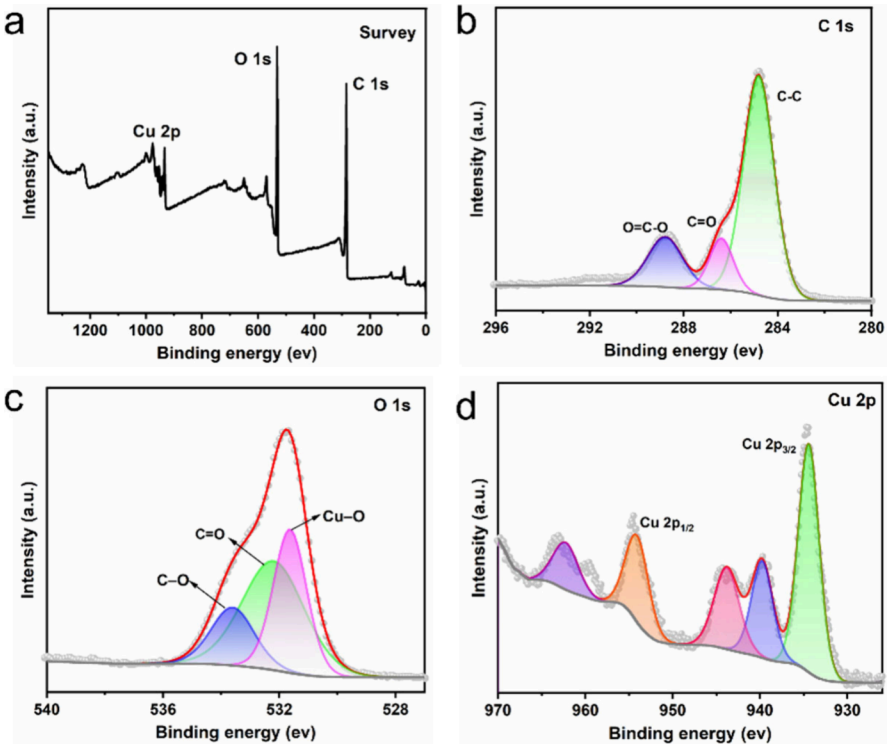


**Figure 3.** XPS survey spectrum of **Cu-OUC** and high-resolution spectra: (a) survey, (b) C 1s, (c) O 1s, and (d) Cu 2p.

defined as a 6-connector and a 3-connector, resulting in the layer being classified as a 2-nodal (3,6)-connected ***kgd*** net with the point (Schläfli) symbol of $(4^3)_2(4^6{\cdot}6^6{\cdot}8^3)$ (Figure 1f).[41]

## Characterizations of Cu-OUC

The FT-IR spectrum showed bands observed between 457 and 584 $cm^{-1}$ as a characteristic of Cu−O bond stretching vibrations (Figure S1). The stretching vibration at 3567−3462 $cm^{-1}$ mainly corresponded to the hydroxyl groups of lattice water molecules in the framework. The characteristic peak of the protonated carboxyl group (1700 $cm^{-1}$) was observed, indicating that the carboxylic acid ligand was partially deprotonated, which was consistent with the crystal structure obtained by SC-XRD. The strong absorption peaks in the range of 1623−1559 $cm^{-1}$ and 1458−1397 $cm^{-1}$ were associated with asymmetric and symmetric bond vibrations of the deprotonated carboxyl group ($COO^-$), respectively, and those notable absorption bands at 1001−1303 $cm^{-1}$ corresponded to the C−O stretching vibration.

The purity of **Cu-OUC** was first confirmed by power X-ray diffraction (PXRD), which showed that the synthesized sample matched well with that of the simulated one in key positions, indicating good phase purity (Figure 2a). Furthermore, the chemical stability of **Cu-OUC** was also tested, where **Cu-OUC** was immersed in acidic and basic aqueous media as well as various organic solvents at room temperature. After 24 h, all PXRD patterns of treated samples closely matched the simulated ones, indicating excellent chemical stability of **Cu-OUC** and ensuring its suitability for further applications. The remarkable chemical stability of **Cu-OUC** is the result of the combination of many aspects, such as the high coordination number of the metal center and the existence of unique clusters.

The thermostability of MOFs is a significant element for their better use in practical applications. Thermogravimetric (TG) analysis was conducted in the temperature range of 30−800 °C to show the thermal behavior of **Cu-OUC** (Figure 2b). In the 30−258 °C temperature range, there is a slight weight loss due to the presence of free water in **Cu-OUC**. Above 258 °C, the structural framework begins to collapse, until the decomposition is complete. TGA showed that the framework of **Cu-OUC** has high thermal stability.

The morphologies of **Cu-OUC** were studied by scanning electron microscopy (SEM), and sheet-like clusters composed of layered structures are shown in Figures 2c and 2d, which coincided with the crystal structure analysis. Furthermore, the structure of **Cu-OUC** was explored through the argon adsorption−desorption test. As shown in Figure S2, **Cu-OUC** showed type III isotherms with an H3 hysteresis loop, indicating the layered structure is mesoporous, which is consistent with the SEM images. The Brunauer−Emmett−Teller surface areas is 5.93 $m^2\ g^{-1}$, with a total pore volume of 0.028 $cm^2\ g^{-1}$, and the main pore size is 19.97 nm, calculated by the Barrett−Joyner−Halenda method. The layered structure and suitable pore size may enhance the exposure of active sites and promote mass diffusion in the catalytic process.

The electronic structure and composition of **Cu-OUC** were evaluated by X-ray photoelectron spectroscopy (XPS). As displayed in Figure 3a, the survey XPS spectra demonstrated the coexistence of Cu, C, and O elements in the as-produced **Cu-OUC** sample. In the high-resolution C 1s spectrum (Figure 3b), three distinct peaks were observed at 288.8, 286.4, and 284.8 eV, which correspond to the =C−O, C=O, and C−C, respectively. The O 1s spectra with peaks at binding energies of 531.3, 532.2, and 533.6 eV were assigned to Cu−O, C=O, and C−O functionalities, respectively (Figure 3c). The peaks at 934.4 and 954.0 eV corresponded to Cu $2p_{3/2}$ and Cu $2p_{1/2}$, respectively (Figure 3d). The peaks at binding energies of 939.8, 943.8, and 962.3 eV belonged to the satellite peaks of Cu $2p_{3/2}$ and Cu $2p_{1/2}$, indicating that Cu(II) was the predominant form of existence in **Cu-OUC**.



https://doi.org/10.1021/jacsau.4c00475
JACS Au 2024, 4, 3823−3832

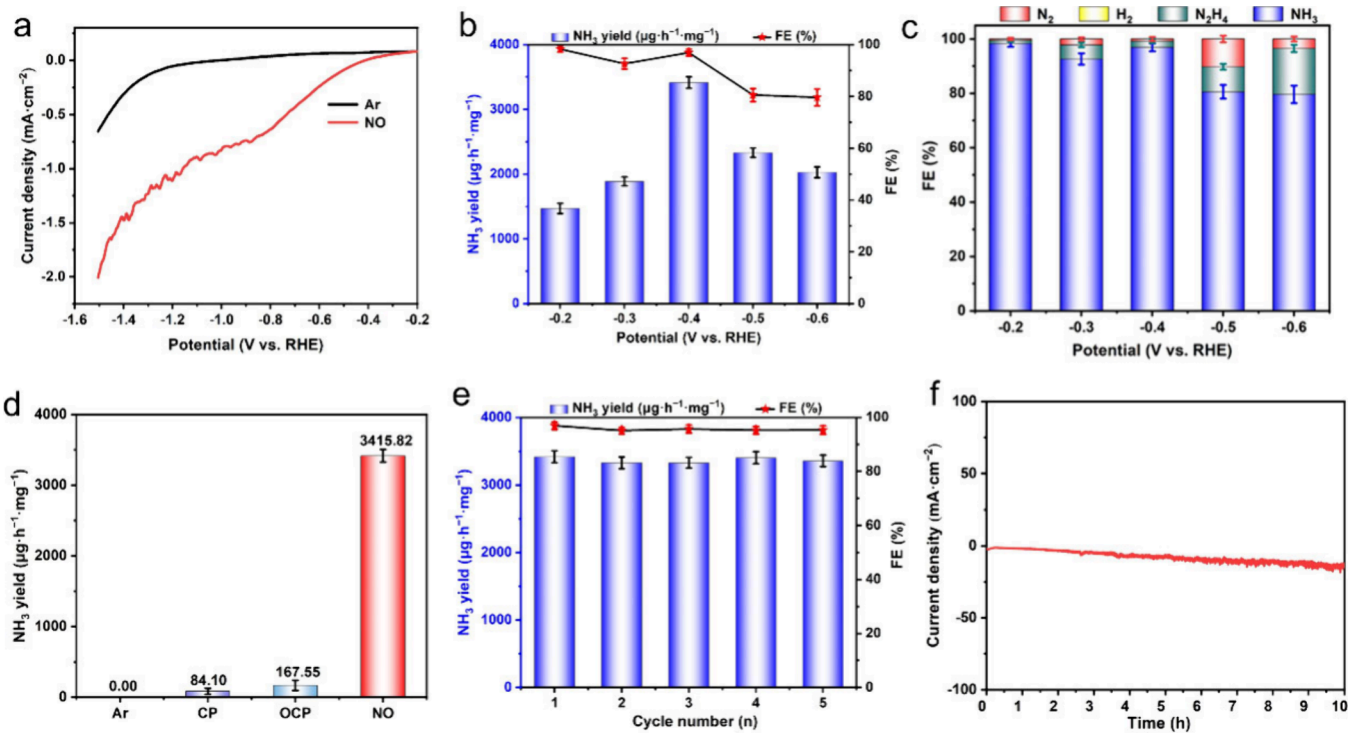


**Figure 4.** (a) LSV of **Cu-OUC** in Ar- and NO-saturated 0.1 M $K_2SO_4$. (b) $NH_3$ yield and Faraday efficiency of **Cu-OUC** at different potentials. (c) The Faraday efficiency of $NH_3$ and byproducts at different potentials. (d) The $NH_3$ yield under different conditions. (e) $NH_3$ yield and Faraday efficiency of **Cu-OUC** at different cycle times of −0.4 V. (f) Current density curve of **Cu-OUC** over time at −0.4 V for 10 h.

## Electrocatalytic NO Reduction Performance

The electrocatalytic NORR performance of **Cu-OUC** was tested in a 0.1 M $K_2SO_4$ saturated NO aqueous solution. **Cu-OUC** was deposited on carbon paper to serve as a working electrode. High-purity argon was initially injected into the electrolytic cell for 0.5 h to purge any possible gas impurities before the electrochemical NORR process. The linear-sweep voltammetry (LSV) for **Cu-OUC** was carried out in electrolytes saturated with Ar and NO, respectively. As displayed in Figure 4a, the current density in the presence of NO is significantly larger than that in the presence of Ar over the potential ranging from −0.20 to −1.50 V, confirming that **Cu-OUC** is catalytically effective toward the NORR, and its performance was further quantitatively evaluated at various potentials by colorimetric analysis[42] (Figure S3). The corresponding UV−vis absorption spectra revealed a gradual increase in peak intensity with the highest value at −0.4 V (Figure S4). The calculated yields of $NH_3$ and FE at various potentials were plotted in Figure 4b. It was found that the as-prepared **Cu-OUC** realized the highest $NH_3$ yield of 3415.82 $\mu g\ h^{-1}\ mg^{-1}$ and FE of 96.91% at −0.40 V, which can serve as one of the most efficient NORR catalysts to date (Table S2).[17,19,43−53] The efficient NORR performance of **Cu-OUC** is attributed to the 2D layered architecture, which provides a highly exposed surface area and active site, shortens the diffusion length of products and reactants, and is beneficial for promoting the electrochemical reaction. However, a further increase in the potential can lead to a significant decrease in NORR activity due to the enhancement of the competing byproduct at elevated potentials. Gas chromatography was employed to measure the quantity of $H_2$, and no $H_2$ is detected at each given potential. The Watt and Chrisp methods[54] were used to detect the byproduct $N_2H_4$ (Figure S5). A small amount of $N_2H_4$ and extremely low FE were detected at different potentials, implying **Cu-OUC** has excellent selectivity toward $NH_3$ synthesis (Figure 4c and Figure S6). Control experiments were conducted to confirm the source of the $NH_3$. As displayed in Figure 4d, the reduction electrolysis tests in the Ar-saturated electrolyte and at open circuit potential (OCP) in the NO-saturated electrolyte offer only trace amounts of $NH_3$. Additionally, bare CP generated $NH_3$ with a negligible yield of 84.10 $\mu g\ h^{-1}\ mg^{-1}$, significantly lower than that of **Cu-OUC**, confirming that **Cu-OUC** acted as the active species for efficient NO conversion to $NH_3$. Thus, it is safe to conclude that the generated $NH_3$ arises exclusively from the NO gas electroreduction catalyzed by **Cu-OUC** under ambient conditions. The catalyst stability or durability is another critical factor for real applications. Recycling tests were conducted at −0.4 V, and **Cu-OUC** exhibited no significant decline in the yield of $NH_3$ and FE over five consecutive NORR cycles, demonstrating the outstanding electrochemical stability of **Cu-OUC** (Figure 4e). The electrocatalytic durability of **Cu-OUC** was further assessed by long-term electrolysis experiments, with a potential of −0.4 V. A steady current density (i.e., electrocatalytic activity) with minor variation was observed over 10 h of continuous chronoamperometry experiments of **Cu-OUC**, and the FE of generated $NH_3$ remained almost unchanged during the stability experiment, stabilizing at 96%, indicating its good durability toward NORR catalysis (Figure 4f and Figures S7 and S8). Moreover, it is evident that the crystal phase and morphology (Figure S9) and structural composition (Figure S10) of **Cu-OUC** were well-preserved before and after electrocatalysis. These results confirm the high electrochemical and mechanical robustness of **Cu-OUC** as an electrocatalyst for the NO-to-$NH_3$ conversion.

## Theoretical Calculations

The theoretical calculations (first-principle density functional theory, DFT) were systematically conducted to get insights into



https://doi.org/10.1021/jacsau.4c00475
JACS Au 2024, 4, 3823−3832

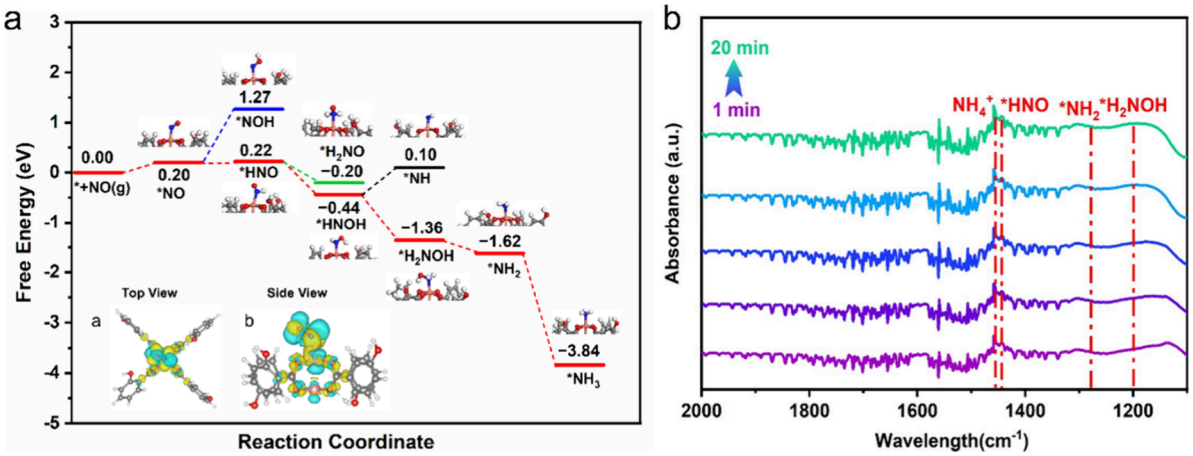


**Figure 5.** (a) Free-energy profiles and intermediate structures for the NORR pathways on **Cu-OUC** (H, white; O, red; Cu, pink; N, blue; C, gray). The charge density differences for the catalyst with adsorbed NO are displayed as insets. The yellow and cyan areas, respectively, represent the accumulation and loss of electrons. The iso-surface value is 0.0008 $e^-$/Bohr$^3$. (b) *In situ* Fourier transform infrared spectroscopy of **Cu-OUC** for the NORR.

NORR catalytic mechanisms over **Cu-OUC**.[55,56] The adsorption of the NO molecule over **Cu-OUC** was initially considered, including the N-end, O-end, and NO-side adsorption configuration. The N-end adsorption configuration gave an adsorption energy of −0.25 eV (calculated based on the active center being the metal center of 2D MOF), and was confirmed as the most stable configuration. Charge density differences showed that when the NO molecule adsorbed on **Cu-OUC**, the charge transfer is a bidirectional process with charge accumulation and depletion observable for both **Cu-OUC** and the NO molecule, which facilitates the activation of NO molecules (insets in Figure 5a). The partial density of states (PDOS) of **Cu-OUC** before and after NO adsorption were further analyzed to reveal **Cu-OUC** and NO interactions (Figure S11). It was found that the partially occupied d-$\pi$* orbitals were formed due to the interaction between Cu 3d orbitals and the $\pi$* orbitals of the NO molecule. Meanwhile, NO $\sigma$ orbitals are hybridized with Cu 3d orbitals under the Fermi level, resulting in the occupied d-$\sigma$ orbitals. Thus, adsorption/activation of NO molecules on **Cu-OUC** may belong to the typical "electron acceptance and donation" mechanism, which denotes that the empty Cu 3d orbitals accept the electrons from the $\sigma$ orbitals of the NO molecule, while the occupied Cu 3d orbitals can back-donate electrons to the empty NO $\pi$* orbitals, similar to other NORR electrocatalysts.[18,19,57,58] Additionally, PDOS analysis also indicates that after adsorbing NO molecules, PDOS states appear in the forbidden band of **Cu-OUC** and the band gap narrows, indicating that it possesses favorable electrical conductivity to enhance electron transfer and improve reaction kinetics, accelerating the activation and reduction of NO during the electrochemical process.[59,60] However, Bader charge analysis shows that the electrons of NO hardly change before and after adsorption, indicating that NO molecules are weakly adsorbed, which can be further supported by integral crystal orbital Hamiltonian population (ICOHP).[61,62] As shown in Figure S12, there are antibonding states filled near the Fermi level, and the ICOHP value is −0.84 eV, indicating weak interactions between **Cu-OUC** and the NO molecule.

The NORR pathway of **Cu-OUC** is further analyzed by Gibbs free energy profiles, starting from the N-end adsorption configuration. As depicted in Figure 5a and Figure S13, the direct hydrogenation of NO molecules to form HNO (NO + $H^+$ + $e^-$ = HNO) gives rise to an uphill energy of 0.63 eV, while the activation step of * + NO(g) to form *NO needs an uphill energy of 0.2 eV due to the weak Cu−N binding between the **Cu-OUC** site and the NO molecule. Thus, thermodynamically, NO molecules are more inclined to adsorb on **Cu-OUC** first before they undergo subsequent hydrogenation reactions. Subsequently, the first protonation of *NO is more favorable for forming *HNO rather than *NOH owing to the lower energy barrier ($\Delta G$) of 0.02 eV. After NO adsorption on the **Cu-OUC**, the d-$\pi$* orbital hybridization around the Fermi level indicates the activation of *NO, which induces low $\Delta G$ for the hydrogenation of *NO to form *HNO. In the following step, *HNO will be further hydrogenated and forms *HNOH or *$H_2$NO species with $\Delta G$ values of −0.66 and −0.42 eV, respectively, demonstrating that the *HNOH species is more energetically favorable to form compared to the formation of *$H_2$NO species. Next, the third proton reacts with *HNOH to achieve *$H_2$NOH with a $\Delta G$ of −0.92 eV, rather than *NH. Further, two successive protonation processes will occur to form *$NH_2$ and *$NH_3$ species, and the $\Delta G$ values for the two steps are −0.26 and −2.22 eV, respectively. Therefore,the NORR on **Cu-OUC** prefers to follow an alternating N pathway (* + NO (g) → *NO → *HNO → *HNOH → *$H_2$NOH → *$NH_2$ → *$NH_3$). For the pathway, the first (* + NO (g) → *NO, with an uphill energy of 0.20 eV) and second (*NO → *HNO, with an uphill energy of 0.02 eV) steps of hydrogenation are endothermic, whereas the subsequent elementary steps are exothermic, indicating that the *NO formation is the potential-limiting step (PDS). It is noteworthy that the PDS barrier (0.20 eV) is lower than that of most catalysts reported previously.[17,43,44,49−53] Furthermore, the intermediates adsorbed on the electrode during the NORR process were captured by electrochemical *in situ* Fourier transform infrared spectroscopy. The enhanced peaks at 1200, 1280, 1446, and 1455 $cm^{-1}$ correspond to *$H_2$NOH, *$NH_2$, *HNO, and $NH_4^+$, respectively. The presence of key intermediates indicates that the NORR pathway of **Cu-OUC** is an alternating N pathway, which is consistent with the results obtained from the theoretical calculations.

Since the HER is the primary competing reaction to the NORR, the competition between the adsorption of *H and *NO on **Cu-OUC** was studied. As seen in Figure S14, the Gibbs


https://doi.org/10.1021/jacsau.4c00475
JACS Au 2024, 4, 3823−3832

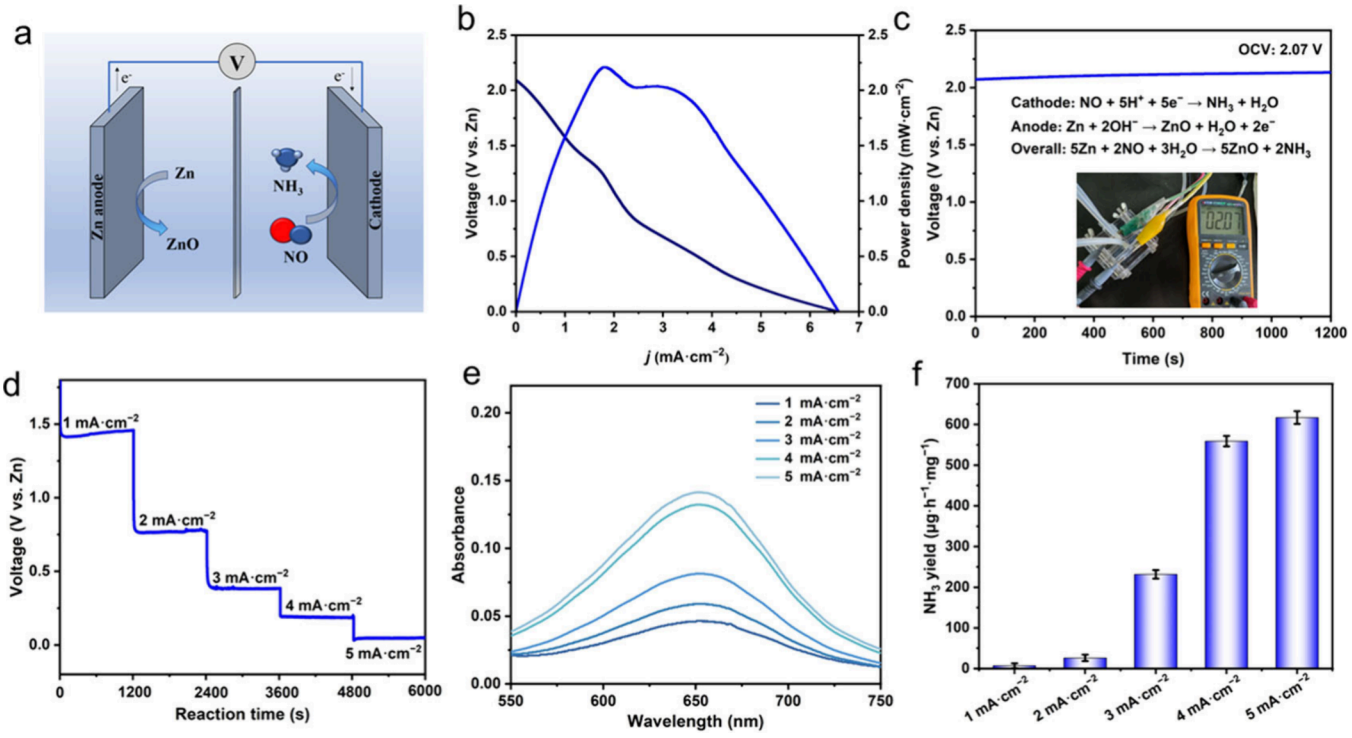


**Figure 6.** (a) Schematic diagram of the Zn−NO primary battery assembled with the **Cu-OUC** cathode. (b) Polarization and power density diagram of the **Cu-OUC** cathode. (c) OCV of the **Cu-OUC** cathode. (d) Discharge tests at different current densities. (e) UV−vis absorption spectra at different currents. (f) $NH_3$ yield under different discharge current densities.

free energy of *H is 1.95 eV on **Cu-OUC**, which is far more positive than that of *NO (0.20 eV), suggesting that the surface of **Cu-OUC** favors the adsorption of *NO over *H, inhibiting the competitive HER and enhancing the NORR selectivity. Therefore, **Cu-OUC** shows excellent selectivity with high Faraday efficiency during the NORR.

### Zn−NO Battery Performance

**Cu-OUC** and a Zn plate served as the cathode catalyst and anode, respectively, to form a proof-of-concept device of an aqueous Zn−NO primary battery, simultaneously reducing NO, generating $NH_3$, and releasing energy. As illustrated in Figure 6a, the Zn anode was converted into ZnO and electrons were released in the discharge process, obtaining electrons on the cathode plate to generate $NH_3$. The established **Cu-OUC**-based battery delivered a power density as high as 2.04 mW $cm^{-2}$ (Figure 6b). It is worth noting that the battery also gave a high open-circuit voltage (OCV) of around 2.07 V versus Zn (Figure 6c) and agreed with the discharging tests. Moreover, the output discharge current density continuously rose from 1.0 to 5.0 mA $cm^{-2}$ around 0.4 V versus Zn, demonstrating that the battery had good discharge capability (Figure 6d). The corresponding UV−vis spectrum of post-NORR electrolytes showed that the $NH_3$ yield rises with the increase of discharge current density (Figure 6e). Finally, the maximum $NH_3$ yield achieved 616.92 $\mu$g $h^{-1}$ $mg^{-1}$, outperforming most recent metal−NO batteries (Figure 6f and Table S3). The Zn−NO battery thus gives rise to opportunities for simultaneous NO abatement, $NH_3$ production, and energy supply.

## CONCLUSIONS

In summary, a 2D copper-based metal−organic framework (**Cu-OUC**) with good chemical and thermal stabilities has been solvothermally obtained, and was experimentally verified as a highly active and durable electrocatalyst for converting NO to $NH_3$ in neutral media. Generally, the electrocatalytic experiments (NORR) showed that **Cu-OUC** can achieve a high FE of up to 96.91% and concurrently give a large $NH_3$ yield as high as 3415.82 $\mu$g $h^{-1}$ $mg^{-1}$. Moreover, the as-prepared **Cu-OUC**/CP-based aqueous Zn−NO battery was also able to present a power density of up to 2.04 mW $cm^{-2}$ and gave an $NH_3$ yield as high as 616.92 $\mu$g $h^{-1}$ $mg^{-1}$. Theoretical investigations were additionally conducted to provide an in-depth understanding of the electrocatalytic NORR mechanism for **Cu-OUC**. The work not only described a promising catalyst having high activity and selectivity for NO-to-$NH_3$ conversion but also provided insights into future design of MOF-based NORR catalysts for $NH_3$ synthesis applications.

## ASSOCIATED CONTENT

### Supporting Information

The Supporting Information is available free of charge at https://pubs.acs.org/doi/10.1021/jacsau.4c00475.

Materials characterizations and methods, X-ray structure determination, calculation details, crystallographic information, performance evaluation, and supplementary data and figures (PDF)

Structure of **Cu-OUC** (CIF)

### Accession Codes

CCDC 2288852 contain the supplementary crystallographic data for this paper. These data can be obtained free of charge via www.ccdc.cam.ac.uk/data_request/cif, or by emailing data_request@ccdc.cam.ac.uk, or by contacting The Cambridge Crystallographic Data Centre, 12 Union Road, Cambridge CB2 1EZ, UK; fax: + 44 1223 336033.



https://doi.org/10.1021/jacsau.4c00475
JACS Au 2024, 4, 3823−3832

## AUTHOR INFORMATION


### Corresponding Authors

**Gui-Lin Zhuang** − *Institute of Industrial Catalysis, State Key Laboratory Breeding Base of Green-Chemical Synthesis Technology, College of Chemical Engineering, Zhejiang University of Technology, Hangzhou 310032, China;* orcid.org/0000-0002-4763-7397; Email: glzhuang@zjut.edu.cn

**Wen-Tai Wang** − *Key Laboratory of Marine Chemistry Theory and Technology, Ministry of Education, College of Chemistry and Chemical Engineering, Ocean University of China, Qingdao 266100, China;* orcid.org/0000-0002-0513-6797; Email: wentaiwang@ouc.edu.cn

**Feng Shao** − *Key Laboratory of Marine Chemistry Theory and Technology, Ministry of Education, College of Chemistry and Chemical Engineering, Ocean University of China, Qingdao 266100, China;* orcid.org/0000-0001-8606-8628; Email: feng.shao@ouc.edu.cn

### Authors

**Rong Luo** − *Key Laboratory of Marine Chemistry Theory and Technology, Ministry of Education, College of Chemistry and Chemical Engineering, Ocean University of China, Qingdao 266100, China*

**Bao-Jing Li** − *Key Laboratory of Marine Chemistry Theory and Technology, Ministry of Education, College of Chemistry and Chemical Engineering, Ocean University of China, Qingdao 266100, China*

**Zhan-Peng Wang** − *Institute of Industrial Catalysis, State Key Laboratory Breeding Base of Green-Chemical Synthesis Technology, College of Chemical Engineering, Zhejiang University of Technology, Hangzhou 310032, China*

**Ming-Guang Chen** − *Baotou Research Institute of Rare Earths, Baotou 014040, China*

**Quan Li** − *Key Laboratory of Marine Chemistry Theory and Technology, Ministry of Education, College of Chemistry and Chemical Engineering, Ocean University of China, Qingdao 266100, China;* orcid.org/0000-0002-1713-879X

**Jia-Ping Tong** − *Laboratory of Physicochemical Analysis, Training Base, Army Logistics Academy, Chongqing 400041, China*

**Yu-Hua Fan** − *Key Laboratory of Marine Chemistry Theory and Technology, Ministry of Education, College of Chemistry and Chemical Engineering, Ocean University of China, Qingdao 266100, China;* orcid.org/0000-0002-5949-3343

Complete contact information is available at: https://pubs.acs.org/10.1021/jacsau.4c00475


### Author Contributions

¶R.L., B.-J.L., and Z.-P.W. contributed equally to this work. CRediT: **Rong Luo** formal analysis, investigation, visualization, writing - original draft; **Bao-Jing Li** data curation, formal analysis, investigation, validation, visualization; **Zhan-Peng Wang** data curation, resources, visualization; **Ming-Guang Chen** formal analysis, validation; **Gui-Lin Zhuang** data curation, formal analysis, resources, software, writing - review & editing; **Jia-Ping Tong** formal analysis; **Wen-Tai Wang** data curation, formal analysis, resources, validation; **Yu-Hua Fan** formal analysis, resources, supervision; **Feng Shao** conceptualization, formal analysis, funding acquisition, project administration, resources, supervision, visualization, writing - review & editing.

### Notes

The authors declare no competing financial interest.

## ACKNOWLEDGMENTS

This work was supported by the Natural Science Foundation of Shandong Province (ZR2021QB140 and ZR2021MB075) and the Fundamental Research Funds for the Central Universities (202113051 and 202364004). G.-L.Z. thanks the support of National Natural Science Foundation of China (22022108 and 22072135). F.S. thanks the Youth Talent Project support (202001013196 and 202101013108) from Ocean University of China, the Open Project support (202017) from the State Key Laboratory of Physical Chemistry of Solid Surfaces, Xiamen University, and the Open Project support (M202317) from the State Key Laboratory of Microbial Technology, Shandong University. F.S. also thanks all the students (name list recorded by OUC ID number as below) in class II of 2022 majoring in chemistry at the Ocean University of China for their kind care and support: Xin-Tong Li, Yan Li, Ying Li, Hai-Feng Liu, Hai-Xia Liu, He-Wei Liu, Jia-Hui Liu, Jia-Peng Liu, Jian-Wei Liu, Jun-Yi Liu, Ke-Jian Liu, Wen-Qi Liu, Xi-Yuan Liu, Xi-Hai Liu, Xu-Jun-Lang Liu, Yan-Wen Liu, Yang Liu, Meng-Di Lu, Zhe Lu, Zhi-Wan Lyu, Jun Ma, Tian-Xuan Ma, Di Mai, Xu-Yan Niu, Zhi-Chao Pan, Bo Peng, Shi-Yi Qiu, Chang-Xiang Ren, Min-Ying Shen, Li-Wei Shi, Pei-Ying Shi, Lei Song, Ce Sun, and Wen-Xu Sun.

## DEDICATION

This work is dedicated to celebrating the first, the 75th, and the century anniversary of Yu-Xiao Shao (Sept 15, 2023), People's Republic of China (Oct 1, 1949), and Ocean University of China (Oct 25, 1924), respectively.

## REFERENCES


(1) Tong, Y.; Guo, H.; Liu, D.; Yan, X.; Su, P.; Liang, J.; Zhou, S.; Liu, J.; Lu, G. Q.; Dou, S. X. Vacancy engineering of iron-doped $W_{18}O_{49}$ nanoreactors for low-barrier electrochemical nitrogen reduction. *Angew. Chem., Int. Ed.* **2020**, *59*, 7356−7361.

(2) Ouyang, L.; Zhou, Q.; Liang, J.; Zhang, L.; Yue, L.; Li, Z.; Li, J.; Luo, Y.; Liu, Q.; Li, N.; Tang, B.; Ali Alshehri, A.; Gong, F.; Sun, X. High-efficiency NO electroreduction to $NH_3$ over honeycomb carbon nanofiber at ambient conditions. *J. Colloid Interface Sci.* **2022**, *616*, 261−267.

(3) Zhao, X.; Hu, G.; Chen, G.-F.; Zhang, H.; Zhang, S.; Wang, H. Comprehensive understanding of the thriving ambient electrochemical nitrogen reduction reaction. *Adv. Mater.* **2021**, *33*, 2007650.

(4) Soloveichik, G. Electrochemical synthesis of ammonia as a potential alternative to the Haber-Bosch process. *Nat. Catal.* **2019**, *2*, 377−380.

(5) Foster, S. L.; Bakovic, S. I. P.; Duda, R. D.; Maheshwari, S.; Milton, R. D.; Minteer, S. D.; Janik, M. J.; Renner, J. N.; Greenlee, L. F. Catalysts for nitrogen reduction to ammonia. *Nat. Catal.* **2018**, *1*, 490−500.

(6) Chen, J. G.; Crooks, R. M.; Seefeldt, L. C.; Bren, K. L.; Bullock, R. M.; Darensbourg, M. Y.; Holland, P. L.; Hoffman, B.; Janik, M. J.; Jones, A. K.; Kanatzidis, M. G.; King, P.; Lancaster, K. M.; Lymar, S. V.; Pfromm, P.; Schneider, W. F.; Schrock, R. R. Beyond fossil fuel-driven nitrogen transformations. *Science* **2018**, *360*, eaar6611.

(7) Liu, D.; Chen, M.; Du, X.; Ai, H.; Lo, K. H.; Wang, S.; Chen, S.; Xing, G.; Wang, X.; Pan, H. Development of electrocatalysts for efficient nitrogen reduction reaction under ambient condition. *Adv. Funct. Mater.* **2021**, *31*, 2008983.

(8) Pang, Y.; Su, C.; Jia, G.; Xu, L.; Shao, Z. Emerging two-dimensional nanomaterials for electrochemical nitrogen reduction. *Chem. Soc. Rev.* **2021**, *50*, 12744−12787.

(9) Zhang, Y.; Wang, Y.; Han, L.; Wang, S.; Cui, T.; Yan, Y.; Xu, M.; Duan, H.; Kuang, Y.; Sun, X. Nitrite electroreduction to ammonia promoted by molecular carbon dioxide with near-unity faradaic efficiency. *Angew. Chem., Int. Ed.* **2023**, *62*, e202213711.
(10) Hao, R.; Tian, L.; Wang, C.; Wang, L.; Liu, Y.; Wang, G.; Li, W.; Ozin, G. A. Pollution to solution: A universal electrocatalyst for reduction of all $NO_x$-based species to $NH_3$. *Chem. Catalysis* **2022**, *2*, 622−638.
(11) Chu, K.; Luo, Y.; Shen, P.; Li, X.; Li, Q.; Guo, Y. Unveiling the synergy of O-vacancy and heterostructure over $MoO_3$-x/MXene for $N_2$ electroreduction to $NH_3$. *Adv. Energy Mater.* **2022**, *12*, 2103022.
(12) Lv, C.; Zhong, L.; Yao, Y.; Liu, D.; Kong, Y.; Jin, X.; Fang, Z.; Xu, W.; Yan, C.; Dinh, K. N.; Shao, M.; Song, L.; Chen, G.; Li, S.; Yan, Q.; Yu, G. Boosting electrocatalytic ammonia production through mimicking "$\pi$ back-donation. *Chem.* **2020**, *6*, 2690−2702.
(13) Li, Y.; Wang, H.; Priest, C.; Li, S.; Xu, P.; Wu, G. Advanced electrocatalysis for energy and environmental sustainability via water and nitrogen reactions. *Adv. Mater.* **2021**, *33*, 2000381.
(14) Wang, M.; Liu, S.; Qian, T.; Liu, J.; Zhou, J.; Ji, H.; Xiong, J.; Zhong, J.; Yan, C. Over 56.55% Faradaic efficiency of ambient ammonia synthesis enabled by positively shifting the reaction potential. *Nat. Commun.* **2019**, *10*, 341.
(15) Zhu, X.; Mou, S.; Peng, Q.; Liu, Q.; Luo, Y.; Chen, G.; Gao, S.; Sun, X. Aqueous electrocatalytic $N_2$ reduction for ambient $NH_3$ synthesis: recent advances in catalyst development and performance improvement. *J. Mater. Chem. A* **2020**, *8*, 1545−1556.
(16) Song, Z.; Liu, Y.; Zhao, J.; Zhong, Y.; Qin, L.; Guo, Q.; Geng, Z.; Zeng, J. Promoting $N_2$ electroreduction into $NH_3$ over porous carbon by introducing oxygen-containing groups. *Chem. Eng. J.* **2022**, *434*, 134636.
(17) Li, Z.; Ma, Z.; Liang, J.; Ren, Y.; Li, T.; Xu, S.; Liu, Q.; Li, N.; Tang, B.; Liu, Y.; Gao, S.; Alshehri, A. A.; Ma, D.; Luo, Y.; Wu, Q.; Sun, X. $MnO_2$ nanoarray with oxygen vacancies: An efficient catalyst for NO electroreduction to $NH_3$ at ambient conditions. *Mater. Today Phys.* **2022**, *22*, 100586.
(18) He, B.; Lv, P.; Wu, D.; Li, X.; Zhu, R.; Chu, K.; Ma, D.; Jia, Y. Confinement catalysis of a single atomic vacancy assisted by aliovalent ion doping enabled efficient NO electroreduction to $NH_3$. *J. Mater. Chem. A* **2022**, *10*, 18690−18700.
(19) Zhang, L.; Liang, J.; Wang, Y.; Mou, T.; Lin, Y.; Yue, L.; Li, T.; Liu, Q.; Luo, Y.; Li, N.; Tang, B.; Liu, Y.; Gao, S.; Alshehri, A. A.; Guo, X.; Ma, D.; Sun, X. High-Performance electrochemical NO reduction into $NH_3$ by $MoS_2$ nanosheet. *Angew. Chem., Int. Ed.* **2021**, *60*, 25263−25268.
(20) Rosca, V.; Duca, M.; de Groot, M. T.; Koper, M. T. M. Nitrogen cycle electrocatalysis. *Chem. Rev.* **2009**, *109* (6), 2209−2244.
(21) de Vooys, A. C. A.; Beltramo, G. L.; van Riet, B.; van Veen, J. A. R.; Koper, M. T. M. Mechanisms of electrochemical reduction and oxidation of nitric oxide. *Electrochim. Acta* **2004**, *49*, 1307−1314.
(22) Farberow, C. A.; Dumesic, J. A.; Mavrikakis, M. Density functional theory calculations and analysis of reaction pathways for reduction of nitric oxide by hydrogen on Pt(111). *ACS Catal.* **2014**, *4*, 3307−3319.
(23) Peng, X.; Mi, Y.; Bao, H.; Liu, Y.; Qi, D.; Qiu, Y.; Zhuo, L.; Zhao, S.; Sun, J.; Tang, X.; Luo, J.; Liu, X. Ambient electrosynthesis of ammonia with efficient denitration. *Nano Energy* **2020**, *78*, 105321.
(24) Liu, L.; Hwang, T.; Lee, S.; Ouyang, Y.; Lee, B.; Smith, S. J.; Tessum, C. W.; Marshall, J. D.; Yan, F.; Daenzer, K.; Bond, T. C. Health and climate impacts of future United States land freight modelled with global-to-urban models. *Nat. Sustain.* **2019**, *2*, 105−112.
(25) Zang, Y.; Wu, Q.; Wang, S.; Huang, B.; Dai, Y.; Ma, Y. High-throughput screening of efficient biatom catalysts based on monolayer carbon nitride for the nitric oxide reduction reaction. *J. Phys. Chem. Lett.* **2022**, *13*, 527−535.
(26) Liu, C.; Li, Q.; Wu, C.; Zhang, J.; Jin, Y.; MacFarlane, D. R.; Sun, C. Single-boron catalysts for nitrogen reduction reaction. *J. Am. Chem. Soc.* **2019**, *141*, 2884−2888.
(27) Jayaramulu, K.; Dubal, D. P.; Schneemann, A.; Ranc, V.; Perez-Reyes, C.; Stráská, J.; Kment, Š.; Otyepka, M.; Fischer, R. A.; Zbořil, R. Shape-assisted 2D MOF/graphene derived hybrids as exceptional lithium-ion battery electrodes. *Adv. Funct. Mater.* **2019**, *29*, 1902539.
(28) Novoselov, K. S.; Geim, A. K.; Morozov, S. V.; Jiang, D.; Zhang, Y.; Dubonos, S. V.; Grigorieva, I. V.; Firsov, A. A. Electric field effect in atomically thin carbon films. *Science* **2004**, *306*, 666−669.
(29) Zeng, X.; Luo, M.; Liu, G.; Wang, X.; Tao, W.; Lin, Y.; Ji, X.; Nie, L.; Mei, L. Polydopamine-modified black phosphorous nanocapsule with enhanced stability and photothermal performance for tumor multimodal treatments. *Adv. Sci.* **2018**, *5*, 1800510.
(30) Su, J.; He, W.; Li, X.-M.; Sun, L.; Wang, H.-Y.; Lan, Y.-Q.; Ding, M.; Zuo, J.-L. High electrical conductivity in a 2D MOF with intrinsic superprotonic conduction and interfacial pseudo-capacitance. *Matter* **2020**, *2*, 711−722.
(31) Chen, L.-F.; Xu, Q. Converting MOFs into amination catalysts. *Science* **2017**, *358*, 304−305.
(32) Liao, P.-Q.; Huang, N.-Y.; Zhang, W.-X.; Zhang, J.-P.; Chen, X.-M. Controlling guest conformation for efficient purification of butadiene. *Science* **2017**, *356*, 1193−1196.
(33) Ren, X.; Liao, G.; Li, Z.; Qiao, H.; Zhang, Y.; Yu, X.; Wang, B.; Tan, H.; Shi, L.; Qi, X.; Zhang, H. Two-dimensional MOF and COF nanosheets for next-generation optoelectronic applications. *Coord. Chem. Rev.* **2021**, *435*, 213781.
(34) Xia, H.; Zhang, J.; Yang, Z.; Guo, S.; Guo, S.; Xu, Q. 2D MOF Nanoflake-assembled spherical microstructures for enhanced supercapacitor and electrocatalysis performances. *Nano-Micro Lett.* **2017**, *9*, 43.
(35) Wang, J.; Li, N.; Xu, Y.; Pang, H. Two-dimensional MOF and COF nanosheets: synthesis and applications in electrochemistry. *Chem.—Eur. J.* **2020**, *26*, 6402.
(36) Cheng, W.; Zhang, H.; Luan, D.; Lou, X. W. Exposing unsaturated $Cu_1$-$O_2$ sites in nanoscale Cu-MOF for efficient electrocatalytic hydrogen evolution. *Sci. Adv.* **2021**, *7*, eabg2580.
(37) Zhu, X.; Huang, H.; Zhang, H.; Zhang, Y.; Shi, P.; Qu, K.; Cheng, S.-B.; Wang, A.-L.; Lu, Q. Filling mesopores of conductive metal-organic frameworks with Cu clusters for selective nitrate reduction to ammonia. *ACS Appl. Mater. Interfaces* **2022**, *14*, 32176−32182.
(38) Xu, Y.; Li, B.; Zheng, S.; Wu, P.; Zhan, J.; Xue, H.; Xu, Q.; Pang, H. Ultrathin two-dimensional cobalt-organic framework nanosheets for high-performance electrocatalytic oxygen evolution. *J. Mater. Chem. A* **2018**, *6*, 22070−22076.
(39) Li, F.; Gu, G.-H.; Choi, C.; Kolla, P.; Hong, S.; Wu, T.-S.; Soo, Y.-L.; Masa, J.; Mukerjee, S.; Jung, Y.; Qiu, J.; Sun, Z. Highly stable two-dimensional bismuth metal-organic frameworks for efficient electrochemical reduction of $CO_2$. *Appl. Catal. B - Environ.* **2020**, *277*, 119241.
(40) Blatov, V. A.; Shevchenko, A. P.; Proserpio, D. M. Applied topological analysis of crystal structures with the program package ToposPro. *Cryst. Growth Des.* **2014**, *14* (7), 3576−3586.
(41) Spek, A. L. Single-crystal structure validation with the program PLATON. *J. Appl. Crystallogr.* **2003**, *36*, 7−13.
(42) Zhu, D.; Zhang, L.; Ruther, R. E.; Hamers, R. J. Photo-illuminated diamond as a solid-state source of solvated electrons in water for nitrogen reduction. *Nat. Mater.* **2013**, *12*, 836−841.
(43) Wang, D.; Chen, Z.-W.; Gu, K.; Chen, C.; Liu, Y.; Wei, X.; Singh, C. V.; Wang, S. Hexagonal cobalt nanosheets for high-performance electrocatalytic NO reduction to $NH_3$. *J. Am. Chem. Soc.* **2023**, *145*, 6899−6904.
(44) Chen, K.; Wang, G.; Guo, Y.; Ma, D.; Chu, K. Iridium single-atom catalyst for highly efficient NO electroreduction to $NH_3$. *Nano Res.* **2023**, *16*, 8737−8742.
(45) Chen, K.; Wang, J.; Kang, J.; Lu, X.; Zhao, X.; Chu, K. Atomically Fe-doped $MoS_{2-x}$ with Fe-Mo dual sites for efficient electrocatalytic NO reduction to $NH_3$. *Appl. Catal., B* **2023**, *324*, 122241.
(46) Liu, Q.; Lin, Y.; Yue, L.; Liang, J.; Zhang, L.; Li, T.; Luo, Y.; Liu, M.; You, J.; Alshehri, A. A.; Kong, Q.; Sun, X. Bi nanoparticles/carbon nanosheet composite: A high-efficiency electrocatalyst for NO reduction to $NH_3$. *Nano Res.* **2022**, *15*, 5032−5037.
(47) Shi, J.; Wang, C.; Yang, R.; Chen, F.; Meng, N.; Yu, Y.; Zhang, B. Promoting nitric oxide electroreduction to ammonia over electron-rich Cu modulated by Ru doping. *Sci. China. Chem.* **2021**, *64*, 1493−1497.


https://doi.org/10.1021/jacsau.4c00475
*JACS Au* 2024, 4, 3823−3832

(48) Liu, P.; Liang, J.; Wang, J.; Zhang, L.; Li, J.; Yue, L.; Ren, Y.; Li, T.; Luo, Y.; Li, N.; Tang, B.; Liu, Q.; Asiri, A. M.; Kong, Q.; Sun, X. High-performance $NH_3$ production via NO electroreduction over a NiO nanosheet array. *Chem. Commun.* **2021**, *57*, 13562−13565.
(49) Liang, J.; Liu, P.; Li, Q.; Li, T.; Yue, L.; Luo, Y.; Liu, Q.; Li, N.; Tang, B.; Alshehri, A. A.; Shakir, I.; Agboola, P. O.; Sun, C.; Sun, X. Amorphous boron carbide on titanium dioxide nanobelt arrays for high efficiency electrocatalytic NO reduction to $NH_3$. *Angew. Chem., Int. Ed.* **2022**, *61*, e202202087.
(50) Li, Y.; Cheng, C.; Han, S.; Huang, Y.; Du, X.; Zhang, B.; Yu, Y. Electrocatalytic reduction of low-concentration nitric oxide into ammonia over Ru nanosheets. *ACS Energy Lett.* **2022**, *7*, 1187−1194.
(51) Mou, T.; Liang, J.; Ma, Z.; Zhang, L.; Lin, Y.; Li, T.; Liu, Q.; Luo, Y.; Liu, Y.; Gao, S.; Zhao, H.; Asiri, A. M.; Ma, D.; Sun, X. High-efficiency electrohydrogenation of nitric oxide to ammonia on a $Ni_2P$ nanoarray under ambient conditions. *J. Mater. Chem. A* **2021**, *9*, 24268−24275.
(52) Liang, J.; Hu, W.-F.; Song, B.; Mou, T.; Zhang, L.; Luo, Y.; Liu, Q.; Alshehri, A. A.; Hamdy, M. S.; Yang, L.-M.; Sun, X. Efficient nitric oxide electroreduction toward ambient ammonia synthesis catalyzed by a CoP nanoarray. *Inorg. Chem. Front.* **2022**, *9*, 1366−1372.
(53) Lin, Y.; Liang, J.; Li, H.; Zhang, L.; Mou, T.; Li, T.; Yue, L.; Ji, Y.; Liu, Q.; Luo, Y.; Li, N.; Tang, B.; Wu, Q.; Hamdy, M. S.; Ma, D.; Sun, X. Bi nanodendrites for highly efficient electrocatalytic NO reduction to $NH_3$ at ambient conditions. *Mater. Today Phys.* **2022**, *22*, 100611.
(54) Watt, G. W.; Chrisp, J. D. Spectrophotometric method for determination of hydrazine. *Anal. Chem.* **1952**, *24*, 2006−2008.
(55) Kresse, G.; Joubert, D. From ultrasoft pseudopotentials to the projector augmented-wave method. *Phys. Rev. B* **1999**, *59*, 1758−1775.
(56) Kresse, G.; Furthmüller, J. Efficient iterative schemes for ab initio total-energy calculations using a plane-wave basis set. *Phys. Rev. B* **1996**, *54*, 11169−11186.
(57) Lv, P.; Wu, D.; He, B.; Li, X.; Zhu, R.; Tang, G.; Lu, Z.; Ma, D.; Jia, Y. An efficient screening strategy towards multifunctional catalysts for the simultaneous electroreduction of $NO_3^-$, $NO_2^-$ and NO to $NH_3$. *J. Mater. Chem. A* **2022**, *10*, 9707−9716.
(58) Niu, H.; Zhang, Z.; Wang, X.; Wan, X.; Kuai, C.; Guo, Y. A feasible strategy for identifying single-Atom catalysts toward electrochemical NO-to-$NH_3$ conversion. *Small* **2021**, *17*, 2102396.
(59) Chu, K.; Li, Q.-q.; Cheng, Y.-h.; Liu, Y.-p. Efficient electrocatalytic nitrogen fixation on $FeMoO_4$ nanorods. *ACS Appl. Mater. Interfaces* **2020**, *12*, 11789−11796.
(60) Li, X.; Chen, K.; Lu, X.; Ma, D.; Chu, K. Atomically dispersed Co catalyst for electrocatalytic NO reduction to $NH_3$. *Chem. Eng. J.* **2023**, *454*, 140333.
(61) Henkelman, G.; Arnaldsson, A.; Jónsson, H. A fast and robust algorithm for Bader decomposition of charge density. *Comput. Mater. Sci.* **2006**, *36*, 354−360.
(62) Dronskowski, R.; Blöchl, P. E. Crystal orbital Hamilton populations (COHP): energy-resolved visualization of chemical bonding in solids based on density-functional calculations. *J. Phys. Chem.* **1993**, *97*, 8617−8624.



https://doi.org/10.1021/jacsau.4c00475
*JACS Au* 2024, 4, 3823−3832